RSC Advances

PAPER

View Article Online
View Journal | View Issue

Cite this: *RSC Adv.*, 2025, **15**, 44145

Synthesis of iron oxide quantum dots by non-thermal atmospheric pressure plasma electrolysis: influence of operating conditions and biomedical applications

K. Navaneetha Pandiyaraj,*[a] M. Karuppusamy,[a] Vandana Chaturvedi Misra,[b] S. Ghorui,[b] A. Raji,[c] P. Saravanan,[d] B. S. Unnikrishnan,[e] P. Gopinath,[e] M. Pichumani,[f] S. Thangamani,[f] S. Yugeswaran,[g] M. C. Ramkumar[h] and Babu Balraj[i]

Iron oxide quantum dots (IOQDs) were synthesized in this work using a distinct non-thermal atmospheric pressure plasma (NTAPP) electrolysis technique. The impact of the operational environment on the synthesis process was thoroughly investigated. The physicochemical properties of the synthesized IOQDs were studied using various methods, including scanning electron microscopy (SEM), transmission electron microscopy (TEM), X-ray photoelectron spectroscopy (XPS), X-ray diffraction (XRD), and vibrating-sample magnetometry (VSM). Further, a time-resolved spectrofluorometer equipped with a time-correlated single photon counting (TCSPC) system was used to measure the photoluminescence lifetime. To explore their potential in biomedical applications, the cytotoxicity and bio-imaging capabilities of the synthesized IOQDs were evaluated through *in vitro* studies using A549 lung adenocarcinoma cells. A significant finding was the predominant presence of magnetite (Fe_3O_4) over hematite (Fe_2O_3) in the IOQDs, which exhibited notable superparamagnetic properties. Interestingly, the specific operating environment during the synthesis process played a crucial role in determining the properties of the IOQDs. The synthesized quantum dots displayed a straightforward biexponential fluorescence decay profile with an average lifetime of 2.02 nanoseconds. The *in vitro* analyses confirmed the non-cytotoxic nature of the IOQDs and highlighted their remarkable bio-imaging potential, underscoring their suitability for integration into various biomedical applications.

Received 24th April 2025
Accepted 27th October 2025

DOI: 10.1039/d5ra02857d

rsc.li/rsc-advances

1. Introduction

Nanotechnology has propelled significant advancements in diverse fields, including electronics, energy storage, environmental remediation, and healthcare, by enabling the design of materials with tailored properties. Among these, magnetic nanomaterials have attracted significant interest due to their unique optical, electrical, and magnetic characteristics. Rapid progress in biomedical technology has been significantly influenced by innovations in nanotechnology, particularly the development of Fe_3O_4 nanoparticles.[1] These nanoparticles are being explored for a range of applications, including hyperthermia under high-frequency magnetic fields, targeted drug delivery, bio-sensing, and T2-contrast enhancement in MRI. Their unique characteristics also make them ideal for therapeutic purposes.[2–6] Fe_3O_4 nanoparticles are known for their excellent biocompatibility,[7] magnetic behavior,[8] and colloidal stability,[9] making them highly effective for bioseparation techniques.[10] Quantum dots (QDs) with sizes ranging from 2 to 10 nm[11] further enhance these capabilities due to their narrow emission spectra,[12] superior photostability,[13] and distinctive chemical properties compared to bulk materials.[14] Several methods, such as sol–gel,[15] microwave,[16] hydrothermal,[17] and solvothermal techniques,[18] have synthesized Fe_3O_4 nanoparticles. However, these conventional approaches face

[a]*Department of Physics, Sri Ramakrishna Mission Vidyalaya College of Arts and Science, Coimbatore 641020, India. E-mail: dr.knpr@gmail.com; Tel: +91-9786452504*

[b]*Laser and Plasma Technology Division, Bhabha Atomic Research Centre, Trombay, Mumbai 400085, India*

[c]*Dr. N.G.P. Institute of Technology, Dr N.G.P. Nagar, Kalapatti Main Road, Coimbatore 641048, India*

[d]*Advanced Magnetics Group, Defence Metallurgical Research Laboratory (DMRL), Hyderabad 500 058, India*

[e]*Nanobiotechnology Laboratory, Centre for Nanotechnology, Indian Institute of Technology Roorkee, Roorkee 247667, Uttarakhand, India*

[f]*Department of Nanoscience and Technology, Sri Ramakrishna Engineering College, Coimbatore 641022, India*

[g]*Department of Physics, Pondicherry University, Puducherry 605014, India*

[h]*Department of Physics, School of Advanced Sciences, Vellore Institute of Technology, Chennai-600127, Tamil Nadu, India*

[i]*Vel Tech Rangarajan Dr Sagunthala R&D Institute of Science and Technology, Chennai, India*

significant challenges, including high temperature requirements, lengthy processing times, excessive chemical usage, and complexity in operation. Moreover, they offer limited control over particle size.[19–22] In contrast, non-thermal atmospheric pressure plasma (NTAPP)-assisted electrolysis has gained attention as a promising alternative for nanoparticle synthesis.[23] In this method, plasma serves as an electrode, introducing electrons and ions into the electrolytic solution. The interaction between NTAPP and the solution creates a highly reactive chemical environment near the plasma–liquid interface, enabling efficient nanoparticle synthesis. This process generates various reactive species, including electrons, radicals, ions, and excited hydroxyl radicals.[24] By adjusting the applied potential and plasma-forming gas, the synthesis process can be precisely controlled, making it a highly versatile technique.

While NTAPP-assisted electrolysis has proven to be a promising method for nanoparticle synthesis, only a handful of studies have focused on its use for producing Fe_3O_4 nanoparticles.[25–28] R. Wang *et al.* synthesized Fe_3O_4 nanoparticles in a liquid medium using non-thermal argon microplasma, achieving an average size of 12.5 nm.[29] H. Nolan *et al.* reported the development of Fe_3O_4 nanoparticles with a size distribution of 9 nm through plasma-assisted electrolysis.[30] Naoki Shirai *et al.* investigated iron oxide nanoparticle synthesis using glow discharge plasma-assisted electrolysis, obtaining particle sizes in the range of 10–20 nm.[31] A previous study by our group demonstrated a novel NTAPP-assisted electrolysis method for synthesizing Fe_3O_4 nanoparticles with an average particle size of 17 nm.[32] However, the development of Fe_3O_4 quantum dots using this approach has not been investigated so far. This study aimed to synthesize Fe_3O_4 quantum dots using NTAP-assisted electrolysis under different processing conditions. The resulting quantum dots were characterized through scanning electron microscopy (SEM), transmission electron microscopy (TEM), X-ray photoelectron spectroscopy (XPS), X-ray diffraction (XRD), and vibrating-sample magnetometry (VSM) to evaluate their morphology, surface chemistry, phase composition, and magnetic properties. Time-resolved fluorescence decay analysis was employed to determine the average lifetime of the Fe_3O_4 quantum dots. Additionally, *in vitro* cytotoxicity and bio-imaging studies were conducted with A549 lung adenocarcinoma cells to explore their potential for biomedical applications.

2. Materials and methods

2.1 Materials

IOQDs were synthesized using commercially available AR grade ferric chloride ($FeCl_3$) and ferrous chloride ($FeCl_2$), both purchased from Sigma-Aldrich, USA. 3-(4,5-Dimethylthiazol-2-yl)-2,5-diphenyltetrazolium bromide (MTT) was also procured from Sigma-Aldrich, USA, while acridine orange (AO) and ethidium bromide (EtBr) were obtained from SRL Pvt. Ltd, India. DMEM/F12 media, Phosphate-Buffered Saline (PBS), and trypsin–EDTA were sourced from Himedia, India. Gibco™ Penicillin-Streptomycin (10 000 U mL^{-1}) and Gibco™ Fetal Bovine Serum (FBS) were acquired from Thermo Fisher Scientific, USA. A549 lung adenocarcinoma cells were purchased from NCCS, Pune, India, and were maintained in DMEM medium with 10% FBS at 37 °C in a 5% CO_2 incubator (NuAire, USA). The cells were sub-cultured once they reached 60% confluence.

2.2 Synthesis of IOQDs

IOQDs were synthesized using a custom designed non-thermal plasma electrolytic reactor, as shown in Fig. 1. The reactor setup comprised of several key components: a plasma torch, high-voltage power source, electrolytic reaction chamber, mass flow controllers (MFCs), gas cylinder, and an iron (Fe) anode. The plasma torch was constructed with a rod-type live electrode measuring 140 mm in length and 4 mm in diameter, paired with a ring-shaped ground electrode made of copper. The inner diameter of the ground electrode was 1.6 cm, while the outer diameter was 2.5 cm. To prevent arc transitions during operation, the live copper electrode was encased in a primary quartz tube and further positioned inside a secondary quartz tube. The ring-shaped ground electrode was also enclosed within a secondary glass tube located just below the live electrode. The distance between the live and ground electrodes was adjustable and fixed at 6 mm for this setup. The torch assembly was enclosed in a Teflon housing to ensure safety and prevent electric induction. This precise design played a crucial role in maintaining the stability and efficiency of the plasma-assisted synthesis process.

The plasma torch unit consists of a specialized gas flow port, with gas flow controlled by a digital mass flow controller (MFC) acquired from Aalborg, USA. The active electrode was connected to a high-voltage power supply capable of delivering a maximum voltage of 40 kV, a current of 50 mA, and a frequency of 50 Hz. The electrolysis process took place in a three-port reaction chamber. At first, the chamber was filled with a prepared electrolytic solution by dissolving 5 mM of $FeCl_3$ and 2.5 mM of $FeCl_2$ in distilled water. Argon gas was bubbled through the solution, and its pH was adjusted to 10 by adding 2 M NaOH. The plasma torch assembly was inserted through the top port of the chamber, maintaining a fixed distance of 1 mm between the solution surface and the torch. The second port was connected to the gas flow unit, which regulated the reaction environment. A separate Fe electrode, acting as the anode, was immersed in the electrolytic solution through the third port, facilitating gas exit. The plasma served as the cathode in this setup, while the Fe rod functioned as the anode. Before the synthesis of IOQDs, the chamber was filled with reactive gases, and argon gas used for plasma formation was introduced between the electrodes *via* MFCs. When a high voltage was applied across the electrodes, a stable plasma jet emerged from the torch orifice and interacted with the electrolytic solution. This interaction initiates various electrochemical reactions at the plasma–liquid interface, including reducing metal cations at the cathode and dissolution reactions at the anode. These processes contributed to the formation of IOQDs at the interface. After synthesis, the crude reaction mixture containing iron oxide quantum dots

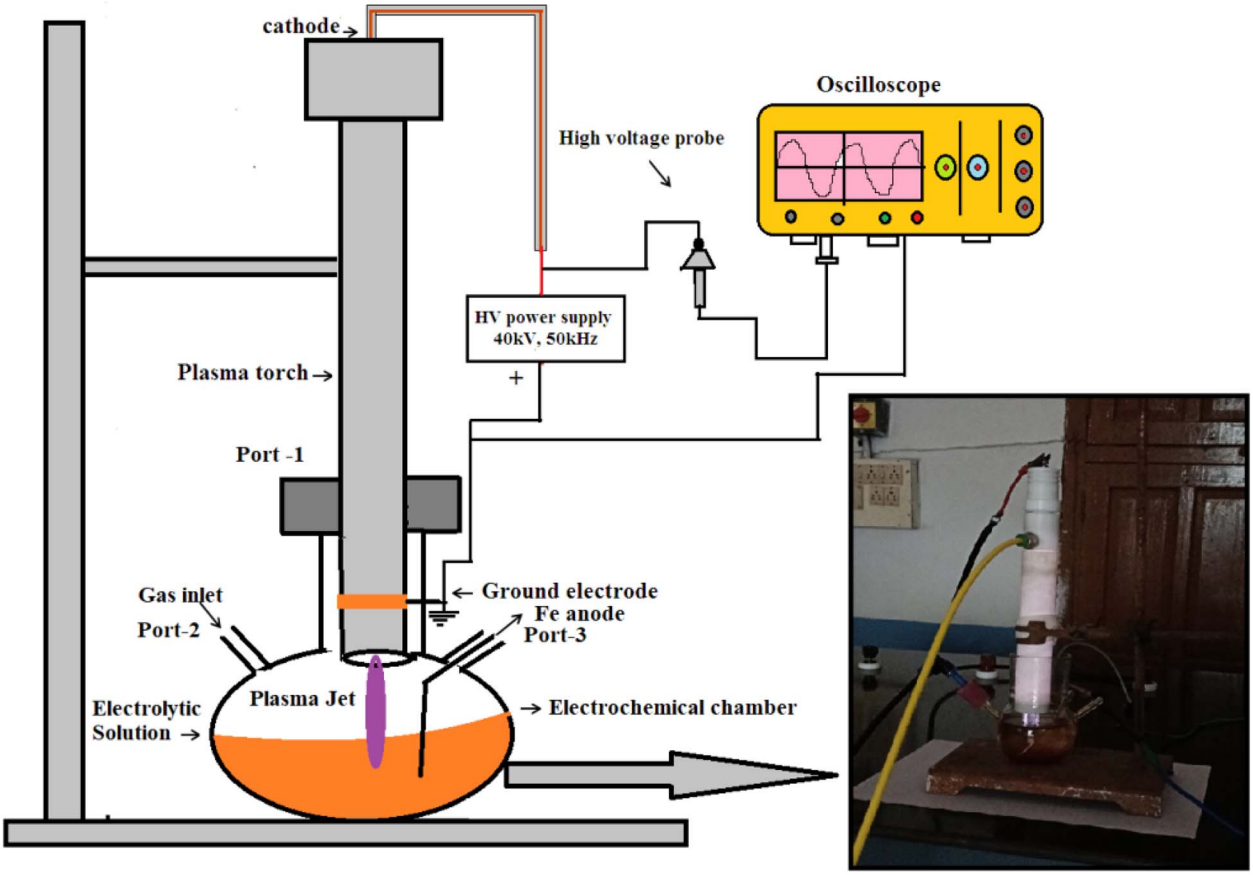

Fig. 1 Schematic diagram of the plasma electrolysis setup.

Table 1 Typical operating parameters used during the plasma process

Working environment	Air, O_2, N_2 and Ar
Plasma forming gas	Ar
Precursors	$FeCl_3$ and $FeCl_2$
Working pressure	Atmospheric pressure
Gas flow Ar	4 lpm
Applied potential	17 kV
Processing time	15 min

(IOQDs) was purified through successive magnetic separation steps. The magnetic fraction was isolated using a neodymium (Nd) magnet to remove unreacted precursors and non-magnetic impurities. The collected material was redispersed in deionized (DI) water and washed three to five times, followed by magnetic decantation to ensure removal of soluble by-products. The resulting dispersion was filtered through Whatman Grade 42 filter paper to eliminate larger aggregates and insoluble residues. The filtrate containing the purified IOQDs was again magnetically collected and subsequently washed four times with DI water and once with ethanol to remove residual ions, surfactants, and organic contaminants and allowed to dry naturally at room temperature for 8–12 hours. The purified IOQDs were finally dried under vacuum at room temperature and stored in airtight containers for further physicochemical, optical, and structural characterisation. The key operational parameters for synthesising IO QDs are summarised in Table 1.

2.3 Characterization of the synthesized IOQDs

The surface chemistry of the synthesized IOQDs was carefully examined using an advanced X-ray photoelectron spectrometer (XPS, ThermiScientific, Al K-Alpha KAN995413). The core level spectra obtained were processed with XPSPEAK 4.1 software, integrated with Lorentz–Gaussian peak shapes for curve fitting to distinguish various chemical bonds within the spectra. FE-SEM was employed with Zeiss Sigma FE-SEM (Germany), which provides high-resolution imaging abilities. TEM analysis was performed using the FEI-TECNAI, G2-20 TWIN at an operating voltage of 200 kV. The particle size distribution was determined at room temperature by a particle size analyzer (Horiba, Ltd, Kyoto, Japan), applying dynamic light scattering. The change in phase of the QDs as a function of the reaction atmosphere was examined through XRD analysis. The Bruker D8 Advance, Panalytical X Pert3, Germany, equipped with 2.2 W K Cu K alpha radiation (λ = 1.54056 Å), was used for this measurement. A vibrating scanning magnetometer (VSM) was used to investigate the magnetic properties of the QDs. The fluorescence lifetime measurements were conducted using a Time-Resolved Spectrofluorometer (Model: Deltaflex, Make:

Horiba, Japan) equipped with a Time-Correlated Single Photon Counting (TCSPC) system. The system features laser diodes with a typical pulse width of 100 ps emitting at 405 nm and 470 nm and a PPD detection module for high-precision measurements. Data acquisition is performed at a rate of up to 1000 TCSPC measurements per second, making it ideal for kinetic and anisotropy studies. To extract decay parameters, the fluorescence decay profiles are analyzed using advanced fitting techniques, such as re-convolution analysis, with measurements ranging from 25 ps to 1 s. Wavelength-dependent decays were also collected for detailed Time-Resolved Emission Spectra (TRES) analysis. This setup ensures robust and precise evaluation of fluorescence dynamics.

2.4 *In vitro* cell assays

2.4.1 Cell viability study. A549 lung adenocarcinoma cells were seeded in a 96-well tissue culture plate at a density of 10^5 cells per well. The plates were incubated at 37 °C in a 5% CO_2 incubator (NuAire, USA) to facilitate cell attachment and growth. After overnight incubation, the cells were exposed to different test samples and incubated again under the same conditions for 24 hours. Following the incubation, 0.1 mL of MTT solution (1 mg mL^{-1} in PBS) was added to each well, and the plates were further incubated at 37 °C for 4 hours in the CO_2 incubator. After this step, the excess dye was carefully removed by aspiration. To dissolve the formazan crystals formed during the assay, 0.1 mL of lysis buffer was added to each well. Using a plate reader Epoch BioTek, Agilent Technologies, the absorbance of the dissolved dye was measured at 570 nm. The cell viability percentage was evaluated using the standard formula.[31]

$$\%\ \text{Cell viability} = \left[\frac{(\text{OD}_{\text{Treated}} - \text{OD}_{\text{Blank}})}{(\text{OD}_{\text{Control}} - \text{OD}_{\text{Blank}})}\right] \times 100 \quad (1)$$

where $OD_{Treated}$, $OD_{Control}$ and OD_{Blank} are the optical density of the treated, control and blank solutions respectively.

2.4.2 Morphological analysis of cell using dual AO-EtBr-staining. A549 lung adenocarcinoma cells were seeded at a density of 10^5 cells/well in a 96- well tissue culture plate and incubated at 37 °C in a 5% CO_2 incubator (NuAire, USA). After overnight incubation, cells were treated with samples at concentration (0.1 mg mL^{-1}). The cells along with the particles were incubated at 37 °C in a 5% CO_2 incubator for 24 h. After incubation time, cells were washed with PBS and incubated with 50 μL of AO/EtBr (1 mg mL^{-1}) solution. Then, the cells were visualized under a phase contrast fluorescence microscope (EVOS M5000, Thermo Fisher Scientific).

2.4.3 *In vitro* cell imaging using fluorescence microscopy. A549 lung adenocarcinoma cells were seeded at a density of 10^5 cells/well in a 96- well tissue culture plate and incubated at 37 °C in a 5% CO_2 incubator (NuAire, USA). Following overnight incubation, the cells were treated with samples. The cells along with the particles were incubated at 37 °C in a 5% CO_2 incubator for 24 h. After incubation period, the cells were washed with PBS, stained with Hoechst 33342/rhodamine 123 and their morphology was visualized under a phase contrast fluorescence microscope.

3. Results and discussion

The synthesis of IOQDs under different atmospheric conditions, including O_2, air, N_2, and Ar, leads to variations in their morphology and structural characteristics. The impact of these

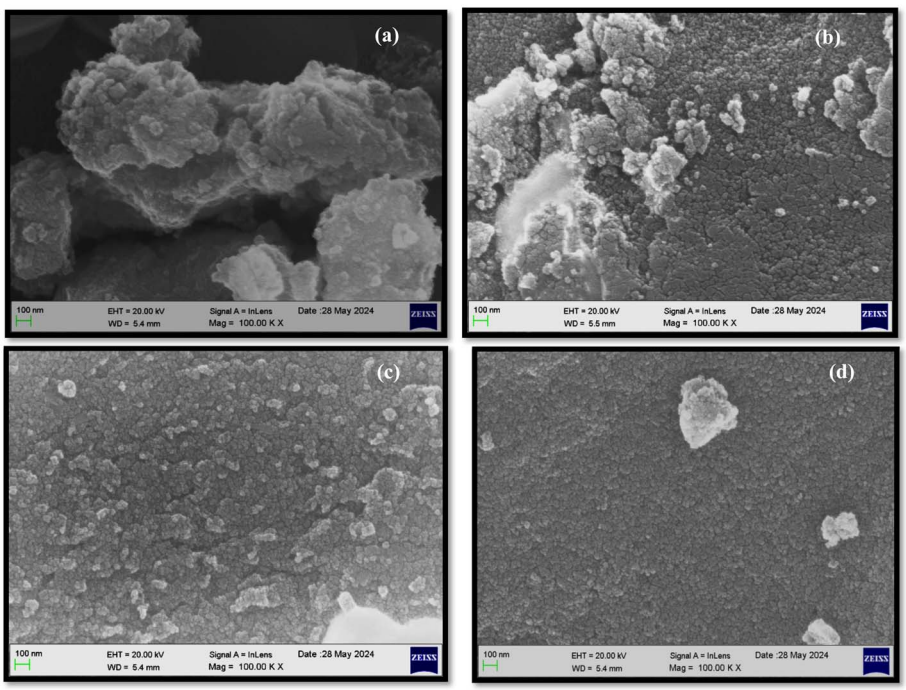

Fig. 2 FE-SEM images of IOQDs synthesized under different environments: (a) O_2, (b) air, (c) N_2, and (d) Ar.

conditions on the particle formation was analyzed using scanning electron microscopy (SEM), X-ray diffraction (XRD), and transmission electron microscopy (TEM). These techniques provide insights into the shape, size, crystallinity, and surface features of the synthesized nanoparticles, allowing for a detailed comparison of the effects of different atmospheric environments on the properties of IOQDs.

3.1 Morphological and structural analysis: SEM, XRD and TEM analysis

Fig. 2 illustrates the morphological evolution of IOQDs synthesized under different atmospheric conditions, including O_2, air, N_2, and Ar. To determine the average particle size, the particle size distribution was analyzed, as shown in Fig. 3. The IOQDs exhibited a generally spherical morphology with a uniform particle size range of 2–7 nm. However, noticeable particle agglomeration was observed in samples synthesized in O_2 and air compared to those produced in N_2 and Ar environments. The average diameter of particles synthesized in an oxygen atmosphere was approximately 3.7 nm. This size progressively decreased in the order of oxygen > air > nitrogen > argon. The particle size obtained from this distribution closely matched the measurements from SEM analysis.

The observed morphological variations can be attributed to the reactive plasma environments. In oxygen and air atmospheres, reactive gaseous species interact with the plasma jet, generating oxygen-containing excited species that transfer to the electrolyte solution. These reactive species further interact with IOQDs formed at the plasma–liquid interface, incorporating oxygen moieties. This incorporation enhances interactions between IOQDs, leading to particle aggregation. In contrast, the Ar and N_2 environments lack oxygen functionalities, resulting in well-defined and separated particles. The SEM findings highlight the significant role of the processing environment in influencing IOQD morphology. Fig. 4 presents the morphology of IOQDs analyzed using TEM. The TEM analysis confirmed a roughly spherical morphology, with an average particle size ranging from 2 to 10 nm (Fig. 4). These results align well with the findings from SEM and particle size distribution analyses.

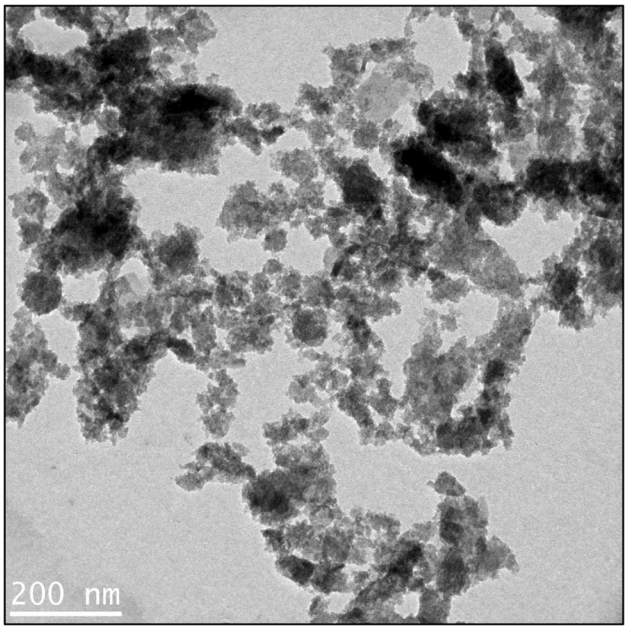

Fig. 4 TEM image of IOQDs synthesized under Ar environment.

The crystallinity of the IOQDs was examined by XRD analysis (Fig. 5). It was observed that no significant signal of Fe_3O_4 was observed in the IOQDs synthesized at all conditions. This may be due to the low crystallinity of IOQDs. Runren Jiang *et al.* observed the similar XRD diffraction pattern of the Fe_3O_4 owing to the lower degree of crystallinity.[33]

3.2 Surface chemistry of IOQDs: XPS analysis

The elemental composition and chemical state of the IOQDs were analyzed using XPS. The survey scan spectra, shown in Fig. 6, reveal the presence of Fe 2p, O 1s, and C 1s peaks on the

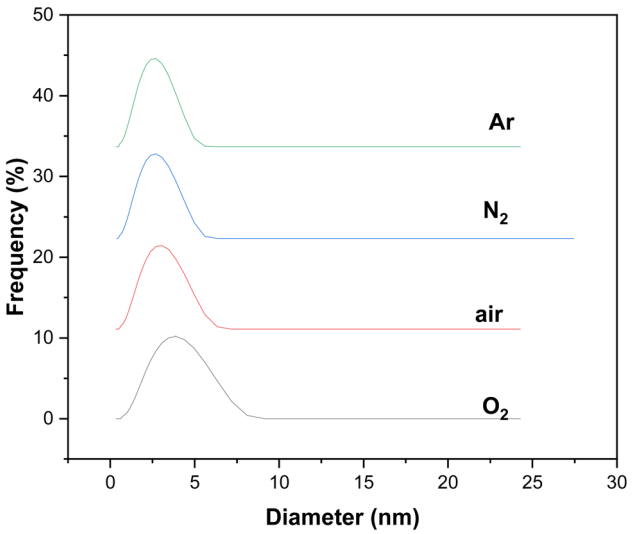

Fig. 3 Variation of particle size distribution of IOQDs synthesized under various environments.

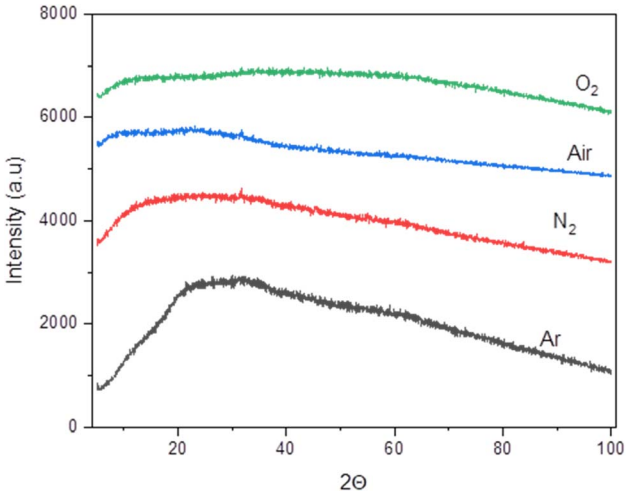

Fig. 5 XRD pattern of IO QDs synthesized under various environments.

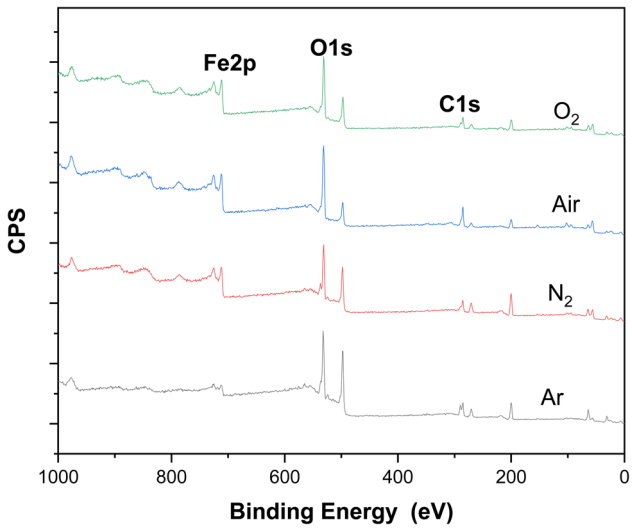

Fig. 6 XPS survey scan spectra of IOQDs synthesized under various environments.

surface of the IOQDs. Additionally, a prominent Na peak was detected, likely originating from the electrolyte solution during the electrolysis process. However, the presence of sodium did not significantly affect the magnetic properties of the IOQDs. The intensity of the Fe 2p peak increased in the order of O_2 < air < N_2 < Ar, while the O 1s component showed a slight decrease. This observation suggests that the Ar and N_2 environments effectively reduce oxidation of the IOQDs, preserving their chemical integrity. The change in the IOQDs chemical state was further examined by deconvolution of the high-resolution Fe 2p spectrum. Fig. 7a shows the Fe 2p high-resolution spectra of the IOQDS synthesized under an O_2 atmosphere. It exhibits two distinct peaks at 711.4 and 724.8 eV attributed to Fe $2p_{3/2}$ and Fe $2p_{1/2}$, indicating the mixed metal oxide of Fe^{2+} and Fe^{3+} respectively. The weak satellite peak was also identified at 719 eV for Fe^{3+}. Fe $2p_{3/2}$ was decomposed into two peaks due to Fe^{2+} and Fe^{3+} oxidation states at 710.2 eV and 713.6 eV. Likewise, the Fe $2p_{1/2}$ peak was further decomposed into two peaks due to Fe^{2+} and Fe^{3+} oxidation states at 723.5 eV and 725.1 eV.[34–37] The difference between Fe $2p_{3/2}$ and Fe $2p_{1/2}$ was calculated at about 13.6 eV indicating the presence of Fe_3O_4 phase.[34–37] The intensity of the peak due to Fe^{3+} oxidation state within both Fe $2p_{1/2}$ and Fe $2p_{3/2}$ was also found to increase significantly on the surface IOQDs synthesized in various environments in order of O_2 <air < Ar < N_2 (Fig. 7b–d). The quantifiable examination of the deconvoluted Fe2p spectra, represented in Fig. 7e endorses these observations. The increase in Fe^{3+} ions in the IOQDs may be attributed to the oxidation of Fe^{3+} and Fe^{2+} ions provided by the submerged iron rod in the electrolytic solution when the processes carried out the O_2 and air environment leads to exhibit the higher concentration of Fe^{3+} ions in the IOQDs. Consequently, the plasma jet allowed a highly energetic electron in the electrolytic solution, which further interacted with the electrolytic solution, generating hydroxyl radicals ($OH^{\bullet}$) at the electrolytic solution–plasma interface. The obtained $OH^{\bullet}$ further reacted with the Fe^{3+} ions in the electrolytic solution, resulting in the formation of Fe^{2+} ions, which further oxidized in the processes carried out in an O_2 and air environment, whereas the Fe^{2+} ions were retained when the processes were carried out in an inert environment. The presence of Fe^{2+}, Fe^{3+} and $OH^{\bullet}$ radicals in the solution contributed to the generation of IOQDs with magnetite phase *via* the following chemical reactions.[29,30]

$$Ar + e^- \rightarrow Ar^* + e^- \quad (2)$$

$$Ar^* + H_2O \rightarrow OH^{\bullet} + H + Ar \quad (3)$$

$$e^- + H_2O \rightarrow OH^{\bullet} + H^{\bullet} + e^- \quad (4)$$

$$OH^{\bullet} + OH^{\bullet} \rightarrow H_2O_2 \quad (5)$$

$$H_2O_2 + Fe^{2+} \rightarrow Fe^{3+} + OH^{\bullet} + OH^- \quad (6)$$

$$Fe^{3+} + e^- \rightarrow Fe^{2+} \quad (7)$$

$$Fe^{3+} + Fe^{2+} + 8OH^- \rightarrow Fe_3O_4 \text{ (magnetite)} + 4H_2O \quad (8)$$

In addition, three major steps are involved in forming IOQDs. Initially, the plasma jet and electrolytic solution interaction provided Fe^{3+} ions, Fe^{2+} ions, and OH radicals. Interaction of OH radicals with Fe ion in the solution promoted the reduction from Fe^{3+} to Fe^{2+} to Fe^0. The reduced Fe-formed nuclei are known as nucleation processes. The nuclei were further integrated with developing nanoparticles to the specific morphology. In the third step, nanoparticles end up being of a constant size and a definite morphology. In this way, the Fe^{3+} ions and Fe^{2+} ions have played significant role in forming nanoparticles with specific phases. Fig. 8 depicts quantifiable information about the various oxygen-containing groups on the surface of IOQDs obtained by deconvolution of the C1s core level spectra of the IOQDs synthesized. The C1s spectra of the IOQDS synthesized at the O_2 atmosphere exhibited four peaks at 285.0 eV, 286.4 eV, 288.0 eV, and 288.9 eV corresponding to C–C/C–H, C–O, C=O and O–C=O groups respectively (Fig. 8a).[38] After IOQDs were synthesized in an air environment, the intensity of the peaks due to C–O, C=O, and O–C=O decreased markedly and further decreased the sample prepared at N_2 and Ar environments (Fig. 8b–d). Fig. 8e shows the relative percentages of the aforementioned functional groups, which quantitatively validated that the amounts of the functional groups (C–O, C=O, and O–C=O) decreased gradually while groups due to C–C/C–H amplified in the order processing environment Ar < N_2 < air < O_2. The observed changes are apparently due to the prevention of the oxidation of IOQDs during the electrolysis, which facilitates the formation Fe^{2+} state rather than the Fe^{3+} state, which is confirmed by the results of Fe 2p spectra.

3.3 Time-correlated single photon studies

The synthesized IOQDs exhibited a fluorescence decay profile characterized by a biexponential fitting curve with an average lifetime of 2.02 ns, as shown in Fig. 9. Chauhan and Watson evaluated fluorescence decay profiles by examining residual

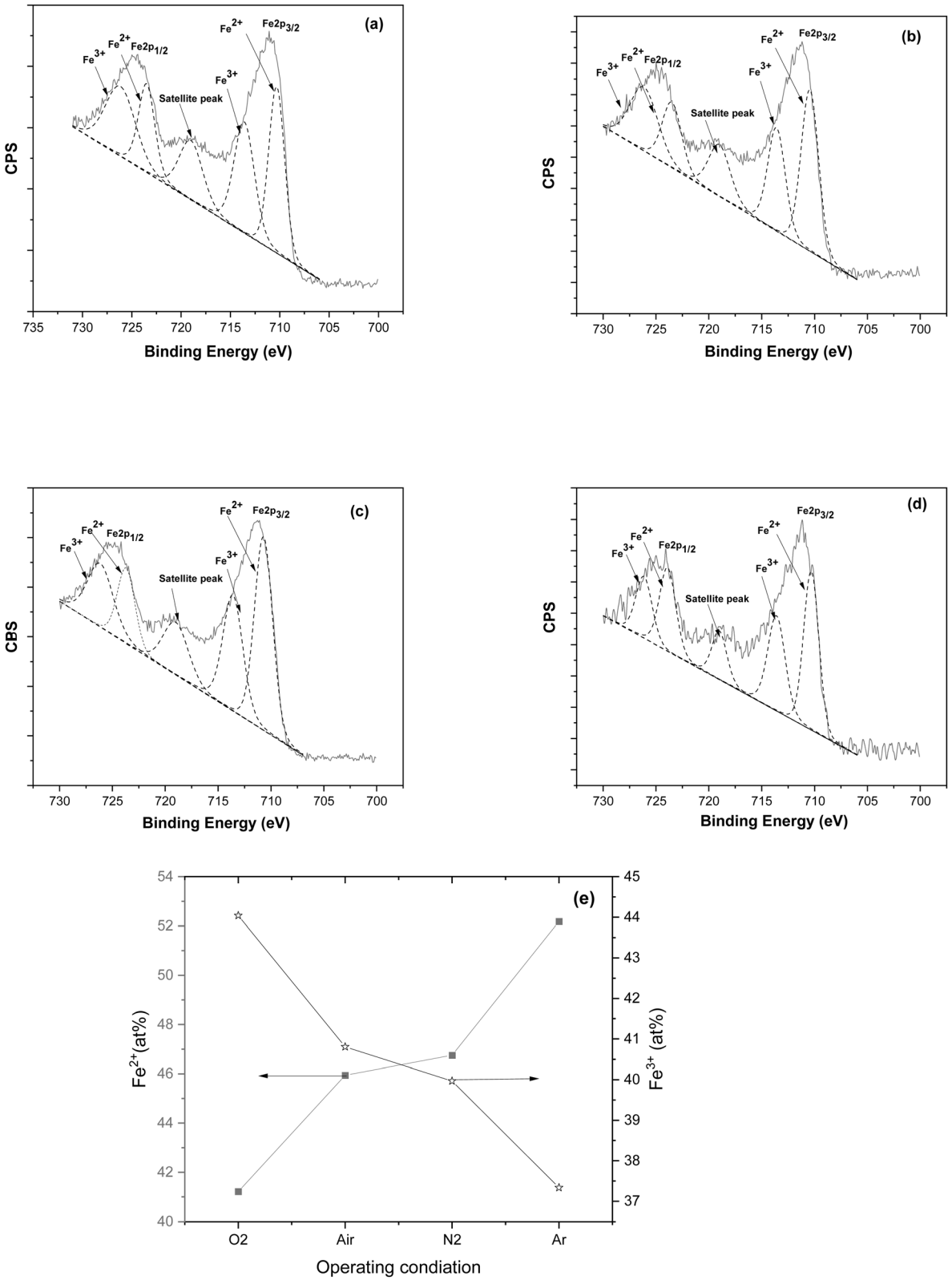

Fig. 7 High-resolution Fe 2p XPS spectra of IOQDs synthesized under different environments: (a) O_2, (b) air, (c) N_2, and (d) Ar. Panel (e) shows the fitted Fe 2p contributions, where peaks corresponding to Fe^{2+} and Fe^{3+} species are deconvoluted and labeled accordingly (Fe^{2+} $2p_{3/2}$, Fe^{3+} $2p_{3/2}$, Fe^{2+} $2p_{1/2}$, Fe^{3+} $2p_{1/2}$, and satellite peaks).

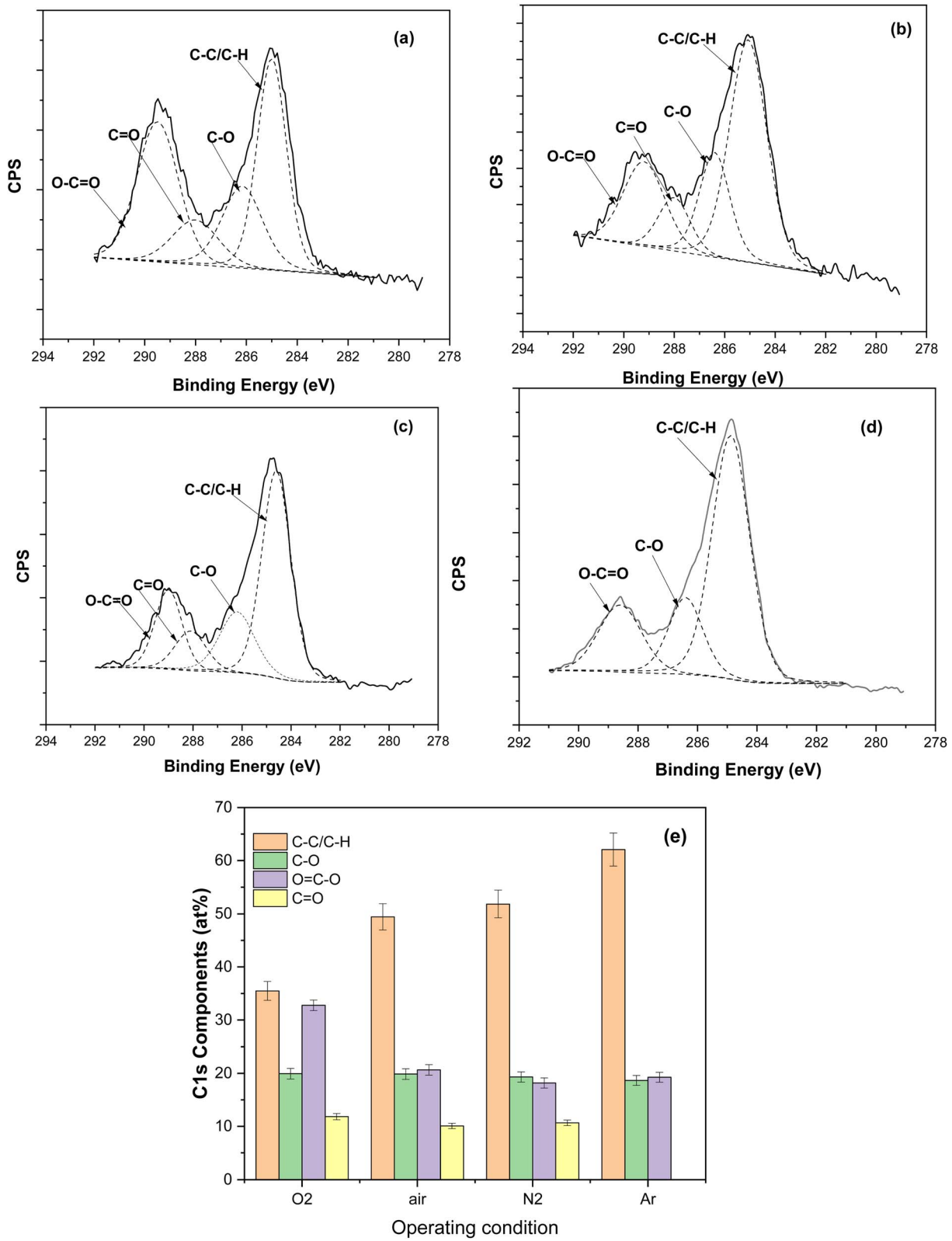

Fig. 8 High-resolution C 1s XPS spectra of IOQDs synthesized under different environments: (a) O_2, (b) air, (c) N_2, and (d) Ar. Panel (e) shows the deconvoluted C1s contributions, including peaks assigned to C–C/C=C (sp^2 carbon), C–O, C=O, and O–C=O functional groups.

distributions and chi-square values, with 0.95 to 1.40 considered an acceptable range.[39] They introduced additional exponential components only when these significantly improved chi-square values and refined residual plots over time. The decay profile of IOQDs yielded a chi-square value of 1.21, confirming the reliability of the fit. In comparison, Sedat Nizamoglu *et al.*

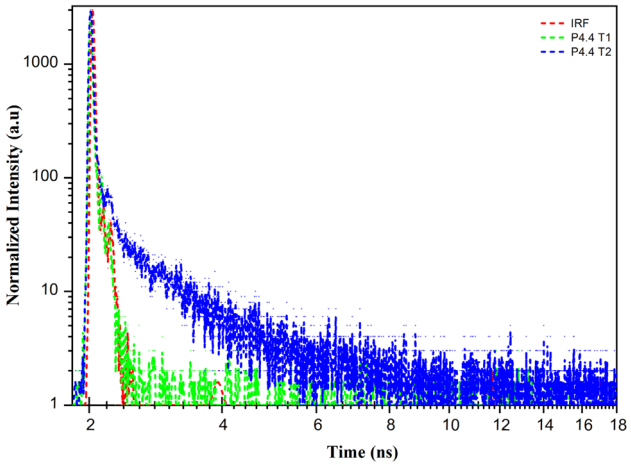

Fig. 9 Fluorescence decay profile showing the instrument response function (IRF, red dashed line) and biexponential decay components (P4.4 T1 in green, P4.4 T2 in blue) with normalized intensity plotted on a semi-log scale as a function of time.

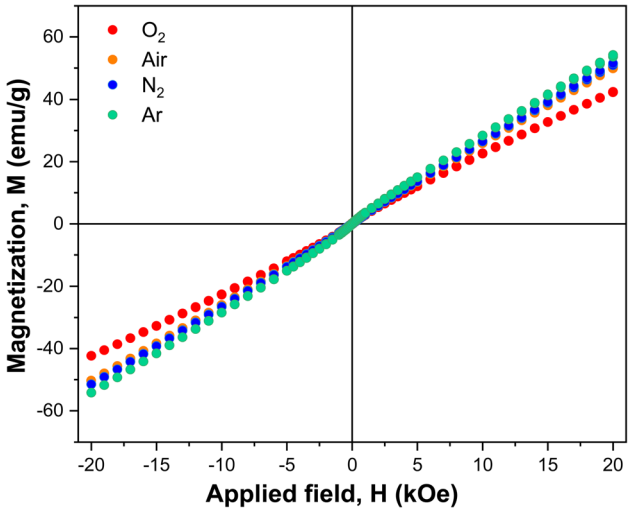

Fig. 11 Magnetization curve of IOQDs synthesized under different environments.

investigated a white-light-emitting hybrid system composed of QWs and QDs, which displayed a multi-exponential decay pattern.[40]

This system included two components corresponding to nanocrystal lifetimes of 12.87 ns and 49.99 ns, along with a short lifetime of 2.00 ns characterized by a negative amplitude, indicative of resonant energy transfer. The chi-square value of 1.0171 confirmed the fit's accuracy. Unlike the hybrid system, which demonstrated complex interactions such as energy transfer, the IOQDs showed a simpler biexponential fluorescence decay with no evidence of multi-component dynamics. Additionally, the IO QDs displayed strong blue fluorescence when illuminated with UV light, as shown in Fig. 10.

3.4 Magnetic properties of the synthesized IOQDs: VSM results

The magnetic properties of the IOQDs were assessed using a Vibrating Sample Magnetometer (VSM) under ambient conditions. Fig. 11 presents the magnetization curves of IOQDs synthesized in different environments. The hysteresis curves shown in the figure indicate the superparamagnetic behavior of the IOQDs across various synthesis conditions. The saturation magnetization (M_s) of IOQDs synthesized in an O_2 atmosphere was measured at 42.65 emu g^{-1}. After synthesizing the IOQDs in different environments, the M_s values were found to increase in the following order: O_2 (42.65 emu g^{-1}) < air (49.25 emu g^{-1}) < N_2) (51.51 emu g^{-1}) < Ar (54.98 emu g^{-1}). This increase in M_s is likely due to a higher presence of Fe^{2+} ions in the IOQDs synthesized under the argon environment, which facilitates the formation of a larger magnetite phase. Aseya Akbar *et al.* reported that an increase in the Fe^{2+} ionic state plays a crucial role in enhancing the magnetite phase, thereby significantly boosting the saturation magnetization.[41] The VSM results strongly support the remarkable superparamagnetic properties of the IOQDs, making these nanoparticles potential candidates for various biomedical applications. Such superparamagnetic iron oxide nanostructures have been widely explored for MRI and targeted drug delivery applications, as reported in recent studies.[42]

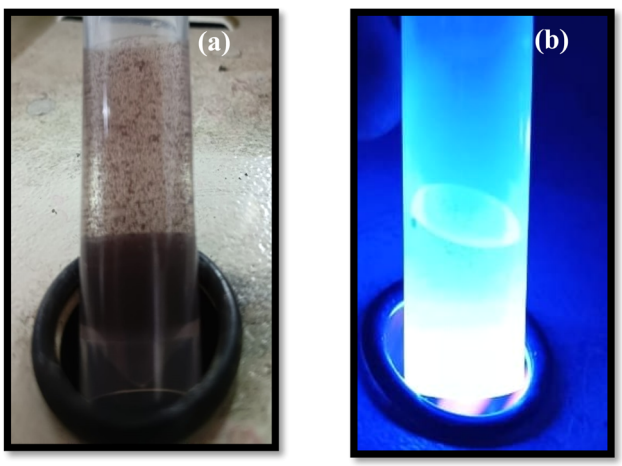

Fig. 10 Photograph of IOQDs (a) before and (b) after illumination of UV light.

3.5 *In vitro* cytocompatability and cell imaging analysis

The cell viability of the synthesized IOQDs in different environments was assessed using the MTT assay with A549 lung adenocarcinoma cells, which serves as an indicator of the toxicity of the IOQDs (Fig. 12). The cell viability of the QDs was compared with the standard tissue culture plate (TCP), which was considered 100%. The results showed that the cell viability of QDs synthesized under an O_2 atmosphere was 52%. For the other environments, the cell viability increased in the following order: O_2 < air < N_2 < Ar. The variation in cytocompatibility of the QDs is likely linked to their phase, particularly the magnetite phase, as well as their particle size.

Previous studies by Xi Zhou *et al.* indicated that IOQDs with a magnetite phase showed significantly higher cell viability

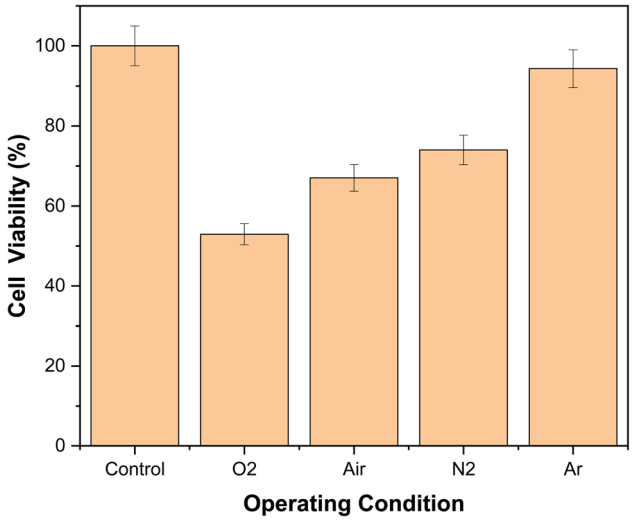

Fig. 12 Cell viability percentage of IOQDs synthesized under various environment.

compared to hematite.[43] In line with this, the IONP QDs synthesized under the Ar atmosphere provided an effective surface for cell adhesion and proliferation, similar to the control (TCP). These non-cytotoxic results, with 99.16% cell viability, highlight the potential of IOQDs as suitable materials for biomedical applications. Our findings are consistent with reports that surface-modified iron oxide nanoparticles exhibit high biocompatibility and negligible cytotoxicity at sub-millimolar concentrations.[44] Additionally, the cell compatibility of the IONP QDs was further evaluated by examining the surface morphology of A549 lung adenocarcinoma cells in Fig. 13.

The cell adhesion, morphology, and proliferation of A549 lung adenocarcinoma cells were cultured in the presence of IOQDs were examined through fluorescence microscopy for an incubation time at 24 h (Fig. 13). The results were compared with those of TCP, which acts as a control. Results showed that all IOQD treated cells emit a high density of green fluorescence, perhaps an indication of significant adhesion and spreading of cells on IOQD surfaces. Furthermore, the cells did not reveal any remarkable changes in morphology (*i.e.*, non-toxic), indicating that adhered cells are healthy, with normal morphology and intact membrane structures. When looking at the images obtained with a red fluorescent filter and displaying the dead/damaged cells stained with EtBr, a few dead/damaged cells were perceived after culturing with IOQDs synthesized under air atmosphere, related to a higher density of live cells.

In order to evaluate the morphology of cells adhering to the IOQDs, HO/RB staining was conducted (Fig. 14). HO is a nuclear stain, while RB labels the cytoplasmic vesicles by binding to AT-rich regions in DNA. In this study, toxicity was assessed by observing the reduction in cytoplasmic or nuclear fluorescence of the stained cells.[45–47] The staining revealed uniform fluorescence in the nucleus and cytoplasm of cells on the IOQDs surface, with no significant decrease in fluorescence emission. However, the nucleus exhibited very weak emission signals. Based on these observations, it can be concluded that the IOQDs are non-toxic and do not cause any harmful effects on cell health. Overall, the *in vitro* cell compatibility analysis reveals that the IOQDs exhibit excellent compatibility under all conditions, making them suitable for use as fluorescence probes or staining agents in bioimaging applications. Beyond bioimaging, the iron oxide core enables them to function as nanozymes. The potential application of magnetic

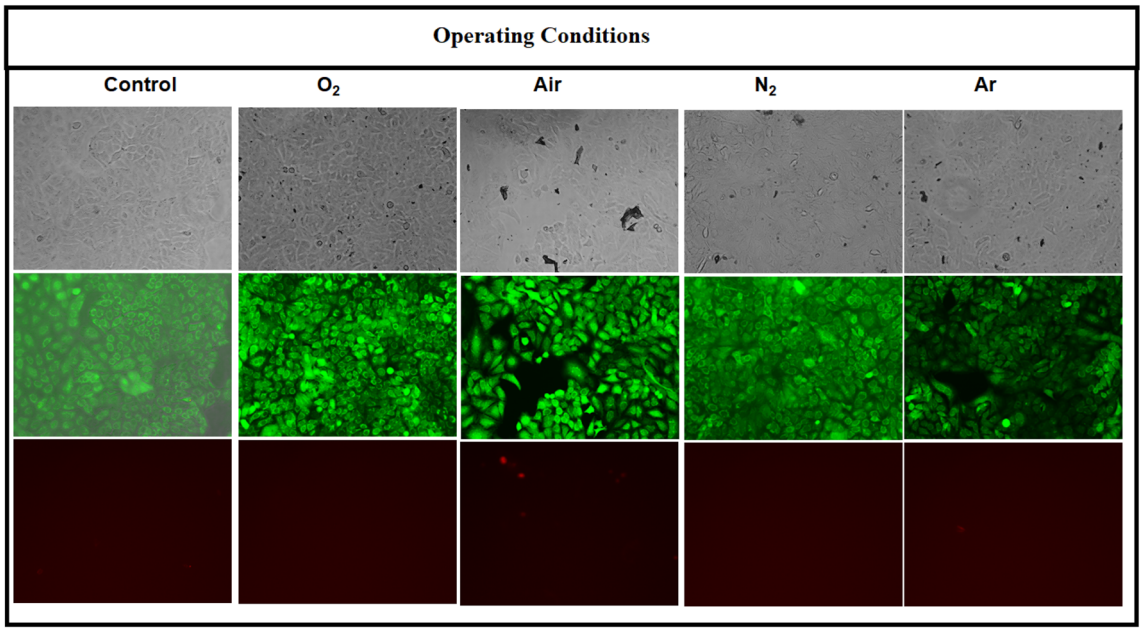

Fig. 13 Phase contract and fluorescent micrographs of A549 lung adenocarcinoma cells subjected to a dual AO/EtBr staining and cultured on a TCP and in the presence of IOQDs synthesized under various environment.

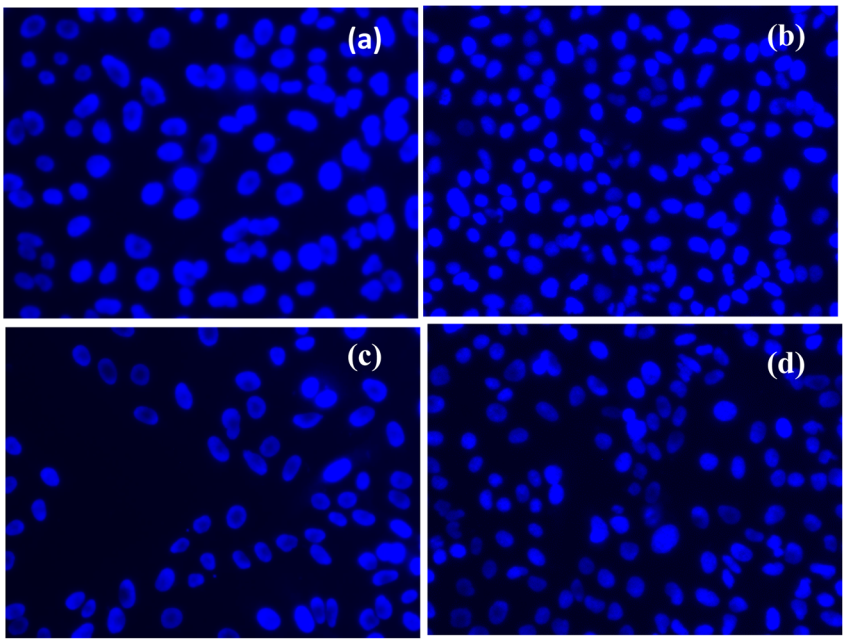

Fig. 14 Fluorescence microscopic images of HO/RB stained A549 lung adenocarcinoma cells in the presence of IOQDs synthesized under various environment (a) O_2, (b) air, (c) N_2 and (d) Ar.

nanoparticles to overcome tumours through catalase-mimicking activity is currently a major focus in cancer nanomedicine.[48] This indicates that IOQDs not only serve as excellent bioimaging agents but also hold significant promise for synergistic cancer therapy applications due to their inherent catalytic properties.

4. Conclusion

This study introduces a novel non-thermal atmospheric pressure plasma electrolysis technique to synthesize IOQDs, exploring various operating environments such as air, O_2, N_2, and Ar. The physicochemical properties of the synthesized IOQDs were thoroughly examined using XPS, XRD, SEM, TEM, and VSM. The photoluminescence lifetime was measured with a Time-Resolved Spectrofluorometer, equipped with a Time-Correlated Single Photon Counting (TCSPC) system. The cytotoxicity and bioimaging potential of the IOQDs were assessed using A549 lung adenocarcinoma cells. XPS analysis confirmed the presence of both Fe_3O_4 and Fe_2O_3 phases in the IOQDs, with a higher concentration of Fe^{2+} oxidation state, indicating the dominance of the magnetite phase. XRD results revealed no significant Fe_3O_4 signals due to the lower crystallinity of the IOQDs. SEM, TEM, and particle size analysis showed that the size of the synthesized IOQDs was approximately 2–4 nm. VSM analysis confirmed the superparamagnetic behavior of the IOQDs, with a saturation magnetization (M_s) value of 54.98 emu g^{-1} for samples synthesized in the Ar environment. The properties of the IOQDs were influenced by the synthesis conditions, with the samples produced under Ar showing the best performance. The fluorescence decay profile of the IOQDs synthesized in the Ar environment followed a simpler biexponential pattern with an average lifetime of 2.02 ns. Finally, *in vitro* studies confirmed the non-cytotoxic nature of the IOQDs and highlighted their potential for bioimaging applications in biomedical fields.

Conflicts of interest

There are no conflicts of interest.

Data availability

The data supporting this article have been included as part of the supplementary information (SI). Supplementary information is available. See DOI: **https://doi.org/10.1039/d5ra02857d**.

Acknowledgements

The corresponding author Dr K. Navaneetha Pandiyaraj would like to acknowledge the Department of Atomic Energy-Board of Research in Nuclear Sciences (DAE-BRNS) (57/14/01/2022 BRNS/34014, dated 01.06.2022), Government of India, for the financial support provided to conduct this research.

References

1 M. J. Molaei and E. Salimi, Magneto-fluorescent superparamagnetic Fe_3O_4@SiO_2@ alginate/carbon quantum dots nanohybrid for drug delivery, *Mater. Chem. Phys.*, 2022, **288**, 126361.
2 Z. Zhang and J. Kong, Novel magnetic Fe3O4@C nanoparticles as adsorbents for removal of organic dyes from aqueous solution, *J. Hazard. Mater.*, 2011, **193**, 325–329.

3 K. R. Wierzbinski, T. Szymanski, N. Rozwadowska, J. D. Rybka, A. Zimna, T. Zalewski, K. Nowicka-Bauer, A. Malcher, M. Nowaczyk, M. Krupinski, M. Fiedorowicz, P. Bogorodzki, P. Grieb, M. Giersig and M. K. Kurpisz, Potential use of superparamagnetic iron oxide nanoparticles for *in vitro* and *in vivo* bioimaging of human myoblasts, *Sci. Rep.*, 2018, **8**(1), 3682.

4 K. C. Barick, S. Singh, D. Bahadur, M. A. Lawande, D. P. Patkar and P. A. Hassan, Carboxyl decorated Fe3O4 nanoparticles for MRI diagnosis and localized hyperthermia, *J. Colloid Interface Sci.*, 2014, **418**, 120–125.

5 S. Sudewi, C. H. Li, S. Dayalan, M. Zulfajri, P. V. S. Sashankh and G. G. Huang, Enhanced fluorescent iron oxide quantum dots for rapid and interference free recognizing lysine in dairy products, *Spectrochim. Acta, Part A*, 2022, **279**, 121453.

6 T. Vangijzegem, D. Stanicki and S. Laurent, Magnetic iron oxide nanoparticles for drug delivery: applications and characteristics, *Expert Opin. Drug Delivery*, 2019, **16**(1), 69–78.

7 D. Chen, Q. Tang, X. Li, X. Zhou, J. Zang, W. Q. Xue, J. Y. Xiang and C. Q. Guo, Biocompatibility of magnetic Fe_3O_4 nanoparticles and their cytotoxic effect on MCF-7 cells, *Int. J. Nanomed.*, 2012, **7**, 4973–4982.

8 M. D. Nguyen, H.-V. Tran, S. Xu and T. R. Lee, Fe3O4 Nanoparticles: Structures, Synthesis, Magnetic Properties, Surface Functionalization, and Emerging Applications, *Appl. Sci.*, 2021, **11**, 11301.

9 H. Wang, X. Zhao, X. Han, Z. Tang, F. Song, S. Zhang, Y. Zhu, W. Guo, Z. He, Q. Guo, F. Wu, X. Meng and J. P. Giesy, Colloidal stability of Fe3O4 magnetic nanoparticles differentially impacted by dissolved organic matter and cations in synthetic and naturally-occurred environmental waters, *Environ. Pollut.*, 2018, **241**, 912–921, DOI: **10.1016/j.envpol.2018.06.029**.

10 J. K. Xu, F. F. Zhang, J. J. Sun, J. Sheng, F. Wang and M. Sun, Bio and nanomaterials based on Fe3O4, *Molecules*, 2014, **19**(12), 21506–21528, DOI: **10.3390/molecules191221506**.

11 H. Park, D. Shin and J. Yu, Categorization of Quantum Dots, Clusters, Nanoclusters, and Nanodots, *J. Chem. Educ.*, 2021, **98**(3), 703–709, DOI: **10.1021/acs.jchemed.0c01403**.

12 M. M. Barroso, Quantum dots in cell biology, *J. Histochem. Cytochem.*, 2011, **59**(3), 237–251, DOI: **10.1369/0022155411398487**.

13 J. Bailes, Photostability of Semiconductor Quantum Dots in Response to UV Exposure, *Methods Mol. Biol.*, 2020, **2118**, 343–349, DOI: **10.1007/978-1-0716-0319-2_25**.

14 T. Mounika, K. Meenu, S. L. Belagali, C. Dharmashekar, K. T. Vadiraj, C. Shivamallu and S. P. Kollur, Ferric oxide quantum dots (FOQDs) for photovoltaic and biological applications: Synthesis and characterization, *Inorg. Chem. Commun.*, 2022, **140**, 109487.

15 Z. Takai, M. Mustafa, S. Asman and K. Sekak, Preparation and Characterization of Magnetite (Fe3O4) nanoparticles By Sol-Gel Method, *Int. J. Nanoelectron. Mater.*, 2019, **12**, 37–46.

16 P. Torkaman, R. Karimzadeh and A. Jafari, Assessment of the synthesis method of Fe3O4 nanocatalysts and its effectiveness in viscosity reduction and heavy oil upgrading, *Sci. Rep.*, 2023, **13**, 18151.

17 S. Ge, X. Shi, K. Sun, C. Li, J. R. Baker, M. M. Banaszak Holl and B. G. Orr, A Facile Hydrothermal Synthesis of Iron Oxide Nanoparticles with Tunable Magnetic Properties, *J. Phys. Chem. C Nanomater. Interfaces*, 2009, **113**(31), 13593–13599, DOI: **10.1021/jp902953t**.

18 J. Xu, Y. Sun and J. Zhang, Solvothermal synthesis of Fe_3O_4 nanospheres for high-performance electrochemical non-enzymatic glucose sensor, *Sci. Rep.*, 2020, **10**, 16026.

19 R. M. Rezaei, H. Razmi, V. Abdollahi and A. A. Matin, Preparation and characterization of Fe3O4/graphene quantum dots nanocomposite as an efficient adsorbent in magnetic solid phase extraction: application to determination of bisphenol A in water samples, *Anal. Methods*, 2014, **6**, 8413.

20 M. D. Rakibuddin and H. Kim, Sol-gel derived Fe_3O_4 quantum dot decorated silica composites for effective removal of arsenic (III) from water, *Mater. Chem. Phys.*, 2020, **240**, 122245.

21 J. Cao, Q. Liu, J. Du, L. Yang, M. Wei, M. Gao and J. Yang, Facile one-step hydrothermal method to fabricate Fe_3O_4 quantum dots–graphene nanocomposites for extraction of dye from aqueous solution, *J. Mater. Sci.: Mater. Electron.*, 2017, **28**, 2267–2271.

22 E. Prathibha, R. Rangasamy, A. Sridhar and K. Lakshmi, Synthesis and Characterization of Fe3O4/Carbon Dot Supported MnO2 Nanoparticles for the Controlled Oxidation of Benzyl Alcohols, *ChemistrySelect*, 2020, **5**, 988–993.

23 P. Lamichhane, R. Paneru, L. Nguyen, J. Lim, P. Bhartiya, B. Adhikari, S. Mumtaz and E. Choi, Plasma-assisted nitrogen fixation in water with various metals, *React. Chem. Eng.*, 2020, **5**, 2053–2057, DOI: **10.1039/D0RE00248H**.

24 M. Barclay, K. Firestein, X. Wang, N. Motta, D. Dubal and K. Ostrikov, Plasma-activated water for improved intercalation and pseudocapacitance of MnO2 supercapacitor electrodes, *Mater. Today Sustain.*, 2023, **22**, 100388, DOI: **10.1016/j.mtsust.2023.100388**.

25 E. R. Kavitha, K. Suresh, S. Yugeswaran and P. Balraju, Ellipsoidal shaped Co_3O_4 quantum dots synthesis by atmospheric microplasma discharge: An electrochemical study, *Mater. Lett.*, 2024, **362**, 136212.

26 E. R. Kavitha, S. Meiyazhagan, S. Yugeswaran and K. Suresh, Expeditious and single step synthesis of ceria quantum dots by microplasma discharge method for supercapacitor applications, *Mater. Chem. Phys.*, 2024, **318**, 129319.

27 C. Richmonds and R. M. Sankaran, Plasma-liquid electrochemistry: Rapid synthesis of colloidal metal nanoparticles by microplasma reduction of aqueous cations, *Appl. Phys. Lett.*, 2008, **93**, 131501.

28 N. Shirai, S. Uchida and F. Tochikubo, Synthesis of metal nanoparticles by dual plasma electrolysis using atmospheric dc glow discharge in contact with liquid, *Jpn. J. Appl. Phys.*, 2014, **53**, 046202.

29 R. Wang, S. Zuo, W. Zhu, J. Zhang and J. Fang, Rapid Synthesis of Aqueous-Phase Magnetite Nanoparticles by

Atmospheric Pressure Non-Thermal Microplasma and their Application in Magnetic Resonance Imaging, *Plasma Processes Polym.*, 2014, **11**, 448–454.

30 H. Nolan, D. Sun, B. G. Falzon, P. Maguire, D. Mariotti, L. Zhang and D. Sun, Thermoresponsive nanocomposites incorporating microplasma synthesized magnetic nanoparticles—Synthesis and potential applications, *Plasma Processes Polym.*, 2019, **16**(2), 1800128.

31 N. Shirai, T. Yoshida, S. Uchida and F. Tochikubo, Synthesis of magnetic nanoparticles by atmospheric-pressure glow discharge plasma-assisted electrolysis, *Jpn. J. Appl. Phys.*, 2017, **56**, 076201.

32 K. N. Pandiyaraj, M. Karuppusamy, P. Jayamurugan, V. C. Misra, S. Ghorui, P. Saravanan, M. N. Nadagouda, B. S. Unnikrishnan, P. Gopinath, M. Pichumani, R. Ghobeira, N. D. Geyter and R. Morent, Iron oxide nanoparticles (IOQDs) synthesized *via* a novel non-thermal atmospheric pressure plasma-assisted electrolysis: Physicochemical characterization and cytocompatibility evaluation, *Adv. Powder Technol.*, 2024, **35**(5), 104441.

33 R. Jiang, D. Wua, G. Lua, Z. Yana, J. Liua, R. Zhoua and M. Nkooma, Fabrication of Fe3O4 quantum dots modified BiOCl/BiVO4 p–n heterojunction to enhance photocatalytic activity for removing broad-spectrum antibiotics under visible light, *J. Taiwan Inst. Chem. Eng.*, 2019, **96**, 681–690.

34 A. D. J. R. Baltazar, Sonochemical activation-assisted biosynthesis of Au/Fe3O4 nanoparticles and sonocatalytic degradation of methyl orange, *Ultrason. Sonochem.*, 2021, **73**, 105521.

35 A. Tayefeha, R. Poursalehi, M. Wiesnerb and S. A. Mousavi, XPS study of size effects of Fe3O4 nanoparticles on crosslinking degree of magnetic TFN membrane, *Polym. Test.*, 2019, **73**, 232–241.

36 A. Rajan, M. Sharma and N. K. Sahu, Assessing magnetic and inductive thermal properties of various surfactants functionalised Fe3O4 nanoparticles for hyperthermia, *Sci. Rep.*, 2020, **10**, 10.

37 X. Ni, J. Zhang, L. Zhao, F. Wang, H. He and P. Dramou, Study of the solvothermal method time variation effects on magnetic iron oxide nanoparticles (Fe3O4) features, *J. Phys. Chem. Solids*, 2022, **169**, 110855.

38 K. N. Pandiyaraj, D. Vasu, R. Ghobeira, P. S. E. Tabaei, N. D. Geyter, R. Morent, M. Pichumani, P. V. A. Padmanabhanan and R. R. Deshmukh, Dye wastewater degradation by the synergetic effect of an atmospheric pressure plasma treatment and the photocatalytic activity of plasma-functionalized Cu–TiO2 nanoparticles, *J. Hazard. Mater.*, 2021, **405**, 124264.

39 S. Chauhan and D. F. Watson, Photoinduced electron transfer from quantum dots to TiO_2: elucidating the involvement of excitonic and surface states, *Phys. Chem. Chem. Phys.*, 2016, **18**, 20466–20475.

40 S. Nizamoglu, E. Sari, J.-H. Baek, I.-H. Lee and H. V. Demir, White light generation by resonant nonradiative energy transfer from epitaxial InGaN/GaN quantum wells to colloidal CdSe/ZnS core/shell quantum dots, *New J. Phys.*, 2008, **10**(12), 123001.

41 A. Akbar, M. Bashir and S. Naseem, Effect of Fe^{3+}/Fe^{2+} Ratio on Superparamagnetic Behavior of Spin Coated Iron Oxide Thin Films August, *IEEE Trans. Magn.*, 2014, **50**(8), 1–4, DOI: 10.1109/TMAG.2014.2312972.

42 Q. Zhang, S. Liu and Y. Wang, Cell-membrane biomimetic nanomedicines for cancer therapy and diagnosis, *Interdiscip. Med.*, 2023, **1**, e20220012.

43 X. Zhou, Y. Shi, L. Ren, S. Bao, Y. Han, S. Wu, H. Zhang, L. Zhong and Q. Zhang, Controllable synthesis, magnetic and biocompatible properties of Fe_3O_4 and a- Fe_2O_3 nanocrystals, *J. Solid State Chem.*, 2012, **196**, 138–144.

44 L. Li, J. Chen, H. Wang, Y. Sun, Y. Liu, C. Zhang and H. Zhu, Cytotoxicity evaluation of engineered nanomaterials: mechanisms and influencing factors, *ACS Nano*, 2023, **17**, 7443–7455.

45 K. N. Pandiyaraj, M. C. Ram Kumar, A. Arun Kumar, P. V. A. Padmanabhan, R. R. Deshmukh, A. Bendavid, P. G. Su, A. Sachdev and P. Gopinath, Cold atmospheric pressure (CAP) plasma assisted tailoring of LDPE film surfaces for enhancement of adhesive and cytocompatible properties: Influence of operating parameters, *Vacuum*, 2016, **130**, 34–47.

46 I. Matai, A. Sachdeva and P. Gopinath, Multicomponent 5-fluorouracil loaded PAMAM stabilized-silver nanocomposites synergistically induce apoptosis in human cancer cells, *Biomater. Sci.*, 2015, **3**, 457–468.

47 A. Sachdev, I. Matai and P. Gopinath, Dual-functional carbon dots-silver@zinc oxide nanocomposite: *In vitro* evaluation of cellular uptake and apoptosis induction, *J. Mater. Chem. B*, 2015, **3**, 1208–1220.

48 Y. Rao, G. Xu, Z. Zhang, W. Wang, C. Zhang, M. Zhao, Y. Qu, W. Li, M. Ji, Y. Liu and Y. LiCCoupling doping, localized surface plasmon resonance toward acidic -preferential catalase-like nanozyme for oxygen-dominated synergistic cancer therapy, *Chem. Eng. J.*, 2023, **465**, 142961.